

Single-Frequency Imaging and Material Characterization using Reconfigurable Reflectarrays

Weite Zhang, Hipolito Gomez-Sousa, Juan Heredia-Juesas, and Jose A. Martinez-Lorenzo, *IEEE Senior Member*

Abstract—In this work, a physical and geometrical optics based single-frequency imaging scheme is proposed for personal screening systems using multiple reconfigurable reflectarrays. This scheme is able to not only reconstruct profiles of potential threat objects on human body, but also identify their materials in terms of their complex relative permittivities. Both simulation and experiment are carried out to detect dielectric objects at a microwave frequency of 24.16 GHz. The object profiles and complex relative permittivities are obtained with both high accuracy and computational efficiency, which show great potentials for security imaging where inspection of human body for threat materials, such as narcotics, explosives, and other types of contraband, is very common.

Index Terms—Physical and geometrical optics, single-frequency imaging, personal screening, reconfigurable reflectarray, profile reconstruction, complex relative permittivity.

I. INTRODUCTION

THE use of electromagnetic (EM) waves in the microwave and millimeter-wave (mm-wave) bands has attracted intensive research interests during the past few decades in a variety of security [1]–[5], medical [6]–[8], industrial [9]–[11], and other important societal [12]–[14] applications. This is because its unique sensing and imaging capabilities. Specifically, at these frequency bands, EM waves are non-ionizing—making them safe to be used in public spaces—and can be used to penetrate optically opaque materials, to create three-dimensional (3D) images, and to characterize and classify a wide range of hazardous materials, such as explosives related threats and other contraband or illicit substances and goods.

Conventional microwave and mm-wave radar imaging systems—such as those working in monostatic, bistatic, and multistatic configurations [15]–[18]—often require the use of a large bandwidth and stringent inter-antenna synchronization to enable coherent imaging, threat detection, and target classification. These characteristics not only makes the imaging of frequency-dispersive objects more challenging, but also they substantially increase the complexity and cost of the multiple transmitting and receiving modules of the system. During the past decade, several imaging systems—based on compressive sensing (CS) theory [5], [19], [20]—have been proposed not only to reduce the hardware complexity but also to achieve a better imaging resolution when compared to that of traditional synthetic aperture radar (SAR) imaging systems

[21]. However, CS algorithms still need intensive digital signal processing (DSP), setting a heavy computational cost at the receiving end, which ultimately precludes from their use in real-time imaging applications.

Recently, a reflectarray system has been able to perform real-time imaging in people-screening applications [22]–[25]. The reflectarray is made of many 1-bit, phase-adaptable patch reflecting antennas [26], [27], which enable multi-scale, beam focusing and imaging of targets located within a region of interest (RoI). Such a system annihilate the software-based computational cost of DSP imaging algorithms by the replacement with hardware-based focused imaging. Additionally, not only it produces high-resolution images but also operates in real-time; this is because the reflectarray is illuminated with a few transceiver antennas excited with a single-frequency continuous-wave (CW) signal. Notwithstanding, the single-frequency scheme only permits its use in near-field regions; which, in this case, has a maximum range of ≈ 2 m.

Designing such reflectarray-based systems is challenging. This is due to the large electrical size of the reflectarray, so that predicting its performance capabilities in each focusing point of the RoI is computationally unfeasible. In [24], an optimized physical optics (PO) method was proposed to simulate a single-reflectarray-based imaging system in a reasonable amount of time. The PO-based simulation platform was successfully used to reconstruct the profile of both dielectric and metallic objects. However, the object permittivity characterization and classification were not addressed in that work. Moreover, new societally-important emerging scenarios require to image even larger targets that, in some cases, may be distributed over a wide region [28]–[30]; in these cases, additional reflectarrays are required to cover the entire imaging domain. Consequently, a more general PO-based method is needed to simulate multi-reflectarray screening systems.

Conventional EM security screening systems often possess high false alarm rates that ultimately result in uncomfortable pat-downs and reduced systems' throughput. One way to cut down these rates is by using the complex permittivities of objects to discriminate them between hazardous and innocuous materials. The complex permittivity can be characterized from the transmitted and received electromagnetic fields by different methods [31]–[41]. However, several drawbacks remain to be addressed before they can be efficiently used in realistic security applications. These include but are not limited to the following: (1) the need to use multiple transceivers or a large frequency bandwidth [31]–[35], which may result in challenging detection and classification of frequency-dispersive objects [36]–[38]; and (2) the need to incorporate the object thickness

W. Zhang is with the Department of Electrical and Computer Engineering, Northeastern University, Boston, MA, 02115 USA.

H. Gomez-Sousa, Juan Heredia-Juesas, and J. A. Martinez-Lorenzo are with the Department of Electrical and Computer Engineering and Department of Mechanical and Industrial Engineering, Northeastern University, Boston, MA, 02115 USA (e-mail: j.martinezlorenzo@neu.edu).

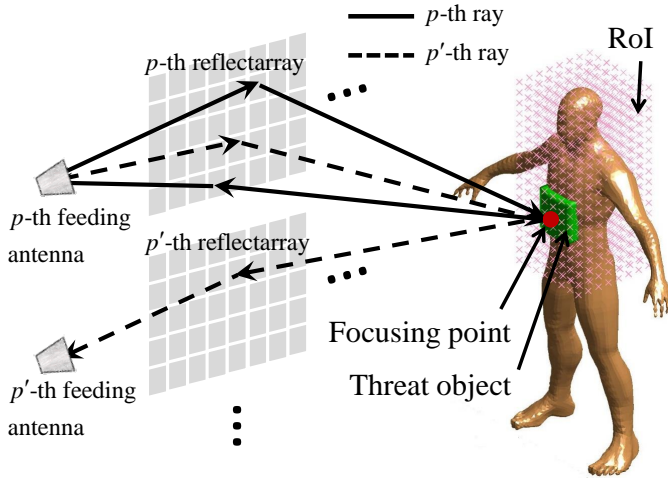


Fig. 1. System concept of microwave screening using multiple reflectarrays at 24.16 GHz, where the p -th feeding antenna is active as a general analysis. The reflectarrays are all confocally configured to focus/refocus the single-frequency CW signal at a specific point, and let it scanned in the RoI. Each reflectarray has a corresponding feeding antenna for transmitting/receiving the radar signal. The concealed dielectric object under detection has an undetermined profile and complex relative permittivity.

[42], [43] or its borders [40], [41] as *prior* information in the estimation process.

In this paper, a single-frequency imaging and material characterization method is proposed for multi-reflectarray systems, requiring no aforementioned object *prior* information. This method is able to not only effectively and efficiently reconstruct the object profile, but also characterize the complex relative permittivity. During the permittivity estimation, which makes use of the range-dependent radiation pattern of the reflectarray in the near-field [44] and considers both the magnitude and phase responses of the received fields, an accurate object thickness can be predicted by solving the phase-shift ambiguity [45]. Such an ambiguity is unavoidable in conventional single-frequency characterization techniques [44], [46], [47], and can lead to a failure in discriminating any two Object- i , $i \in \{1, 2\}$, that satisfy $T_1 \sqrt{\epsilon_1'} = T_2 \sqrt{\epsilon_2'}$, T_i and ϵ_i' being the thickness and the dielectric constant of Object- i , respectively.

The rest of the paper is organized as follows: in Section II, the concept of personal screening systems using multiple active reflectarrays is briefly described. In Section III, a general imaging theory for reconstructing object profiles (using PO) and material characterization (using geometrical optics, GO) is derived. In Section IV, two-reflectarray-based computational simulations and experimental validations are carried out to detect dielectric slabs placed on the surface of a metallic plate at the a frequency of 24.16 GHz. The results show the efficacy of the proposed method to image object profiles and estimate their complex relative permittivities. Section V summarizes the conclusions of this work.

II. SYSTEM CONCEPT

The original idea of using multiple active reflectarrays in people-screening system was pioneered by Smiths Detection

[22]. As is described in Fig. 1, the system has two principal components: (1) the feeding antennas that are used to transmit and receive the single-frequency CW radar signal; and (2) the reflectarrays that are used to focus the CW signal at a point in the RoI, when used in transmission mode, and to refocus the scattered field from that point into to the receiving antennas, when used in receiving mode. In this setup, a potentially concealed dielectric object in the RoI has an unknown profile and a complex relative permittivity of $\epsilon_r = \epsilon_r' - j\epsilon_r''$, where ϵ_r' and ϵ_r'' are the dielectric constant and loss factor, respectively.

Note that each reflectarray is equipped with a single horn antenna and transceiver module, and several reflectarrays can be confocally configured to simultaneously focus at the same point in space and to perform the imaging. In the general configuration shown in Fig. 1, all P pairs of feeding-antenna and reflectarrays (FARAs) are used as follows. First, the CW signal from the p -th feeding antenna is used to illuminate its corresponding reflectarray. Then, this incident field is reflected from the reflectarray and focused at a point in the RoI; this is done by applying a binary phase to each reflectarray patch to make the free space propagation phase of each horn/patch/focusing-point ray to be as close as possible to zero [48]–[50]. Next, the focused incident field interacts with the object, thus producing a new field that is scattered towards the imaging system. Due to the confocal configuration, the scattered field is refocused through the p' -th receiving reflectarray towards its corresponding receiving antenna. Repeating the above procedure for all pairs of transmitting and receiving FARAs, an image of the target under test is finally created. It is important to note that the use of multiple FARAs provide a multiplexing gain that enhances the performance of the imaging system, when compared to the single FARA system described in Ref. [24].

In the following Sections, the microwave operation frequency f_0 is selected to be 24.16 GHz. Because, at that frequency, clothing is essentially transparent, the human body is highly reflective, and dielectric materials are easily identifiable against the body [23]. The body is reasonably assumed to be a perfect electric conductor (PEC) plate.

III. IMAGING THEORY

A. Profile Reconstruction

To get the simulated target profile, all surfaces of the feeding horn apertures, patches on the reflectarrays, and target are discretized into triangular facets. According to the exact free-space near-field equation described in [51], the incident electric field $\mathbf{E}_{\text{inc}}(\mathbf{r})$ and magnetic field $\mathbf{H}_{\text{inc}}(\mathbf{r})$ at an observation point \mathbf{r} can be computed using the electric $\mathbf{J}(\mathbf{r}')$ and magnetic $\mathbf{M}(\mathbf{r}')$ current sources, namely,

$$\begin{aligned} \mathbf{E}_{\text{inc}}(\mathbf{r}) &= \int_S \{-A_1 G_1 \mathbf{J}(\mathbf{r}') - A_1 G_2 [\mathbf{J}(\mathbf{r}') \cdot \mathbf{R}] \mathbf{R} - \\ &\quad B_1 G_3 \mathbf{M}(\mathbf{r}') \times \mathbf{R}\} e^{-jk_0 R} dS \\ \mathbf{H}_{\text{inc}}(\mathbf{r}) &= \int_S \{-A_2 G_1 \mathbf{M}(\mathbf{r}') - A_2 G_2 [\mathbf{M}(\mathbf{r}') \cdot \mathbf{R}] \mathbf{R} + \\ &\quad B_2 G_3 \mathbf{J}(\mathbf{r}') \times \mathbf{R}\} e^{-jk_0 R} dS, \end{aligned} \quad (1)$$

where $A_1 = \frac{j\eta_0}{4\pi k_0}$; $A_2 = \frac{j}{4\pi k_0 \eta_0^2}$; $B_1 = B_2 = \frac{1}{4\pi}$; $G_1 = \frac{-1-jk_0 R+(k_0 R)^2}{R^3}$; $G_2 = \frac{3+j3k_0 R-(k_0 R)^2}{R^5}$; $G_3 = \frac{1+jk_0 R}{R^3}$; $\mathbf{R} = \mathbf{r}-\mathbf{r}'$, $R = |\mathbf{R}|$; k_0 and η_0 are the wave number and impedance in free-space, respectively; \mathbf{r} is the observation point; \mathbf{r}' is the source point; and S is surface of the feeding antenna aperture.

With the incident fields \mathbf{E}_{inc} and \mathbf{H}_{inc} , the induced electric \mathbf{J} and magnetic \mathbf{M} currents on any interface can be calculated using the modified equivalent current approximation (MECA) equations [52], [53], which represents a generalization of the PO for both conducting and non-conducting dielectric surfaces:

$$\mathbf{J}(\mathbf{r}) = \frac{1}{\eta_1} \left[E_{\text{inc}}^{\text{TE}} \cos \theta_{\text{inc}} (1 - R_{\text{TE}}) \hat{\mathbf{e}}_{\text{TE}} + E_{\text{inc}}^{\text{TM}} (1 - R_{\text{TM}}) (\hat{\mathbf{n}}_0 \times \hat{\mathbf{e}}_{\text{TM}}) \right] \Big|_{S_B} \quad (2)$$

$$\mathbf{M}(\mathbf{r}) = E_{\text{inc}}^{\text{TE}} (1 + R_{\text{TE}}) (\hat{\mathbf{e}}_{\text{TM}} \times \hat{\mathbf{n}}_0) + E_{\text{inc}}^{\text{TM}} \cos \theta_{\text{inc}} (1 + R_{\text{TM}}) \hat{\mathbf{e}}_{\text{TE}} \Big|_{S_B},$$

where the incident electric field is decomposed into its transverse electric (TE) and transverse magnetic (TM) modes, and analyzed individually; S_B is the interface between the two media; η_1 is the wave impedance of the outwards medium; $\hat{\mathbf{n}}_0$ is the outward unit vector perpendicular to the interface; θ_{inc} is the incident angle; $E_{\text{inc}}^{\text{TE/TM}}$ and $\hat{\mathbf{e}}_{\text{TE/TM}}$ are the incident field magnitude and the corresponding unit vector of the TE/TM mode, respectively; and $R_{\text{TE/TM}}$ is the reflection coefficient of the TE/TM mode on the interface, which is defined as

$$R_{\text{TE}} \Big|_{\mu_1=\mu_2} = \frac{\cos \theta_{\text{inc}} - \sqrt{\frac{\varepsilon_2}{\varepsilon_1}} \sqrt{1 - \frac{\varepsilon_1}{\varepsilon_2} \sin^2 \theta_{\text{inc}}}}{\cos \theta_{\text{inc}} + \sqrt{\frac{\varepsilon_2}{\varepsilon_1}} \sqrt{1 - \frac{\varepsilon_1}{\varepsilon_2} \sin^2 \theta_{\text{inc}}}} \quad (3)$$

$$R_{\text{TM}} \Big|_{\mu_1=\mu_2} = \frac{-\cos \theta_{\text{inc}} + \sqrt{\frac{\varepsilon_1}{\varepsilon_2}} \sqrt{1 - \frac{\varepsilon_1}{\varepsilon_2} \sin^2 \theta_{\text{inc}}}}{\cos \theta_{\text{inc}} + \sqrt{\frac{\varepsilon_1}{\varepsilon_2}} \sqrt{1 - \frac{\varepsilon_1}{\varepsilon_2} \sin^2 \theta_{\text{inc}}}},$$

where ε_1 and ε_2 are the complex permittivity of the outwards and inner medium, respectively, and μ_1 and μ_2 are the corresponding permeabilities assumed to be equal. Note that on the surface of the PEC, magnetic current $\mathbf{M} = 0$ due to the fact that $R_{\text{TE}} = R_{\text{TM}} = -1$. Therefore, the magnetic currents on the feeding antenna apertures, the patch elements on the reflectarrays, and the human body are neglected.

As shown in Fig. 2, assuming the total number of the patches on each reflectarray is M and the electric current distribution of p -th feeding antenna is $\mathbf{J}_p^{\text{inc}}$ ($p \in \{1, 2, \dots, P\}$), the incident electric $\mathbf{E}_{m,p}^{\text{patch}}$ and magnetic $\mathbf{H}_{m,p}^{\text{patch}}$ fields on the m -th patch ($m \in \{1, 2, \dots, M\}$) can be obtained using Eq. (1). The corresponding induced electric current $\mathbf{J}_{m,p}^{\text{patch}}$ can be calculated based on Eq. (2).

The reflectarrays are confocally set to focus the incident wave front to a desired point by using the binary phase approximation, namely, introducing a phase compensation $\Delta\psi_{n,m,p}$ to each patch element,

$$\Delta\psi_{n,m,p} = \begin{cases} \pi, & \frac{\pi}{2} < \text{mod}(k_0 \cdot L_{n,m,p}, 2\pi) < \frac{3\pi}{2} \\ 0, & \text{otherwise} \end{cases}, \quad (4)$$

where $\text{mod}(\cdot)$ is the modulus operator, and $L_{n,m,p} = (|\mathbf{r}_p^{\text{feed}} - \mathbf{r}_{m,p}^{\text{patch}}| + |\mathbf{r}_{m,p}^{\text{patch}} - \mathbf{r}_n^{\text{focus}}|)$. $\mathbf{r}_p^{\text{feed}}$, $\mathbf{r}_{m,p}^{\text{patch}}$, and $\mathbf{r}_n^{\text{focus}}$

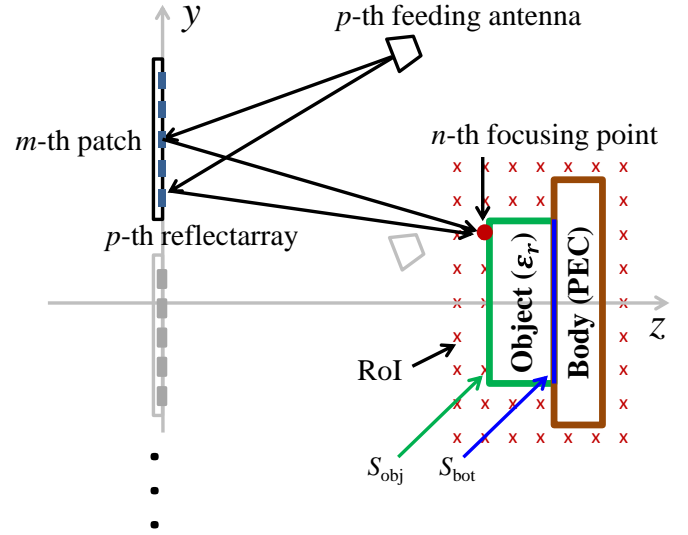


Fig. 2. Simulation model for the reconstruction of the threat profile. The body is assumed to be a PEC plate, and the threat, attached on the body surface, is a dielectric slab with undetermined profile and material in terms of the complex relative permittivity ε_r . S_{obj} and S_{bot} represent the air-object and object-body interface, respectively.

are the positions of the p -th feeding antenna, the m -th patch of the p -th reflectarray, and the n -th focusing point, respectively. Therefore, the electric current is modified as $\mathbf{J}_{m,p}^{\text{patch}} e^{j\Delta\psi_{n,m,p}}$. Using Eq. (1) again, we can calculate the incident electric $\mathbf{E}_{m,n,p}^{\text{target}}$ and magnetic $\mathbf{H}_{m,n,p}^{\text{target}}$ fields on the target surface. Thus, the total incident electric $\mathbf{E}_{n,p}^{\text{target}}$ and magnetic $\mathbf{H}_{n,p}^{\text{target}}$ fields for the p -th feeding antenna and the n -th focusing point are

$$\mathbf{E}_{n,p}^{\text{target}} = \sum_{m=1}^M \mathbf{E}_{m,n,p}^{\text{target}} \quad (5)$$

$$\mathbf{H}_{n,p}^{\text{target}} = \sum_{m=1}^M \mathbf{H}_{m,n,p}^{\text{target}}.$$

According to Eq. (2), the corresponding induced electric $\mathbf{J}_{n,p}^{\text{target}}$ and magnetic $\mathbf{M}_{n,p}^{\text{target}}$ currents can be written as

$$\mathbf{J}_{n,p}^{\text{target}} = \mathbf{J}_{n,p}^{\text{obj}} + \mathbf{J}_{n,p}^{\text{body}} \quad (6)$$

$$\mathbf{M}_{n,p}^{\text{target}} = \mathbf{M}_{n,p}^{\text{obj}} + \mathbf{M}_{n,p}^{\text{body}},$$

where $\mathbf{J}_{n,p}^{\text{obj}}$ and $\mathbf{M}_{n,p}^{\text{obj}}$ are the electric and magnetic currents, respectively, on the surface of the dielectric object. Similarly, $\mathbf{J}_{n,p}^{\text{body}}$ and $\mathbf{M}_{n,p}^{\text{body}}$ are the currents on the surface of the human body. Noticing that $\mathbf{M}_{n,p}^{\text{body}} = 0$ for the human body (approximated to be PEC), one can calculate $\mathbf{J}_{n,p}^{\text{body}}$ using 1st-order PO method. While $\mathbf{J}/\mathbf{M}_{n,p}^{\text{obj}}$ must be calculated considering multiple reflections within the dielectric object using a K^{th} -order PO method based on Eq. (1) and Eq. (2). The process can be described as

$$\begin{aligned} & \mathbf{J}/\mathbf{M}_{n,p,0}^{\text{obj}} \rightarrow \mathbf{E}/\mathbf{H}_{n,p,1}^{\text{bot}} \rightarrow \mathbf{J}/\mathbf{M}_{n,p,1}^{\text{bot}} \rightarrow \mathbf{E}/\mathbf{H}_{n,p,1}^{\text{obj}} \\ & \rightarrow \mathbf{J}/\mathbf{M}_{n,p,1}^{\text{obj}} \rightarrow \mathbf{E}/\mathbf{H}_{n,p,2}^{\text{bot}} \rightarrow \mathbf{J}/\mathbf{M}_{n,p,2}^{\text{bot}} \rightarrow \mathbf{E}/\mathbf{H}_{n,p,2}^{\text{obj}} \\ & \rightarrow \mathbf{J}/\mathbf{M}_{n,p,2}^{\text{obj}} \rightarrow \mathbf{E}/\mathbf{H}_{n,p,3}^{\text{bot}} \rightarrow \mathbf{J}/\mathbf{M}_{n,p,3}^{\text{bot}} \rightarrow \mathbf{E}/\mathbf{H}_{n,p,3}^{\text{obj}} \quad (7) \\ & \vdots \\ & \rightarrow \mathbf{J}/\mathbf{M}_{n,p,K-1}^{\text{obj}} \end{aligned}$$

where $\mathbf{J}/\mathbf{M}_{n,p,0}^{\text{obj}}$ is denoted as the electric or magnetic currents induced by the initial reflection on the air-object interface S_{obj} ; $\mathbf{E}/\mathbf{H}_{n,p,k}^{\text{bot}}$ and $\mathbf{J}/\mathbf{M}_{n,p,k}^{\text{bot}}$ are the incident fields and the induced currents, respectively, on the object-body interface S_{bot} after k ($k \in \{1, 2, \dots, K-1\}$) reflections within the dielectric object; Similarly, $\mathbf{E}/\mathbf{H}_{n,p,k}^{\text{obj}}$ and $\mathbf{J}/\mathbf{M}_{n,p,k}^{\text{obj}}$ correspond to the incident fields and the induced currents, respectively, on S_{obj} . Consequently, the total electric $\mathbf{J}_{n,p}^{\text{obj}}$ and magnetic $\mathbf{M}_{n,p}^{\text{obj}}$ currents on S_{obj} are computed by

$$\begin{aligned} \mathbf{J}_{n,p}^{\text{obj}} &= \mathbf{J}_{n,p,0}^{\text{obj}} - \sum_{k=1}^{K-1} \mathbf{J}_{n,p,k}^{\text{obj}} \\ \mathbf{M}_{n,p}^{\text{obj}} &= \mathbf{M}_{n,p,0}^{\text{obj}} - \sum_{k=1}^{K-1} \mathbf{M}_{n,p,k}^{\text{obj}}. \end{aligned} \quad (8)$$

As all the reflectarrays are confocally arranged, all the receiving antennas are able to receive the scattered signal. Define $\mathbf{E}_{n,p}^{\text{rec}}$ as the total received electric field from the p -th receiving antenna with all P feeding antennas active and the beam focused at the n -th point. Although, $\mathbf{E}_{n,p}^{\text{rec}}$ can be calculated via an inverse computational procedure using the PO method from the target to the receiving horns based on Eq. (1) and Eq. (2), in order to improve the computational efficiency, the general reciprocity theorem for multiple-in-multiple-out (MIMO) systems is used as follows:

$$E_{n,p}^{\text{rec}} = \frac{\int_S \mathbf{E}_{n,p}^{\text{target}} \cdot \mathbf{J}_n^{\text{target}} - \mathbf{H}_{n,p}^{\text{target}} \cdot \mathbf{M}_n^{\text{target}} ds}{\int_S \hat{\mathbf{e}}_{n,p}^{\text{rec}} \cdot \mathbf{J}_p^{\text{inc}} ds}, \quad (9)$$

where $E_{n,p}^{\text{rec}}$ is the amplitude of the received field $\mathbf{E}_{n,p}^{\text{rec}}$, considered to be uniform on the receiving apertures; $\mathbf{J}_n^{\text{target}} = \sum_{p=1}^P \mathbf{J}_{n,p}^{\text{target}}$ and $\mathbf{M}_n^{\text{target}} = \sum_{p=1}^P \mathbf{M}_{n,p}^{\text{target}}$ are the total induced electric and magnetic currents on the target surface, respectively; and $\hat{\mathbf{e}}_{n,p}^{\text{rec}}$ represents the uniform complex polarization vector of $\mathbf{E}_{n,p}^{\text{rec}}$.

Finally, the target profile can be reconstructed by adding the received electric field $E_{n,p}^{\text{rec}}$ from all P receivers,

$$E_n^{\text{rec}} = \sum_{p=1}^P E_{n,p}^{\text{rec}}, \quad (10)$$

and determining the location of the maximum total received field along the z -axis, namely,

$$z_n^{\text{imaging}}(x_n, y_n) = \max_{z_n} \{|E_n^{\text{rec}}(x_n, y_n, z_n)|\}, \quad (11)$$

where (x_n, y_n, z_n) is the location of the n -th focusing point.

B. Material Identification

To ensure real-time prediction and classification of potential threat objects in the reflectarray screening system, it is desired to develop a fully analytical forward model for characterizing the complex relative permittivity of the object under detection [54], [55]. To achieve this, a ray tracing based GO method is proposed to predict the received electric fields \hat{E}_n^{rec} [56]. By sweeping the relative permittivity $\epsilon_r = \epsilon_r' - j\epsilon_r''$ and the object thickness T , $\hat{E}_n^{\text{rec}}(\epsilon_r', \epsilon_r'', T)$ are calculated and compared to the measured E_n^{rec} (or simulated with the full-wave method

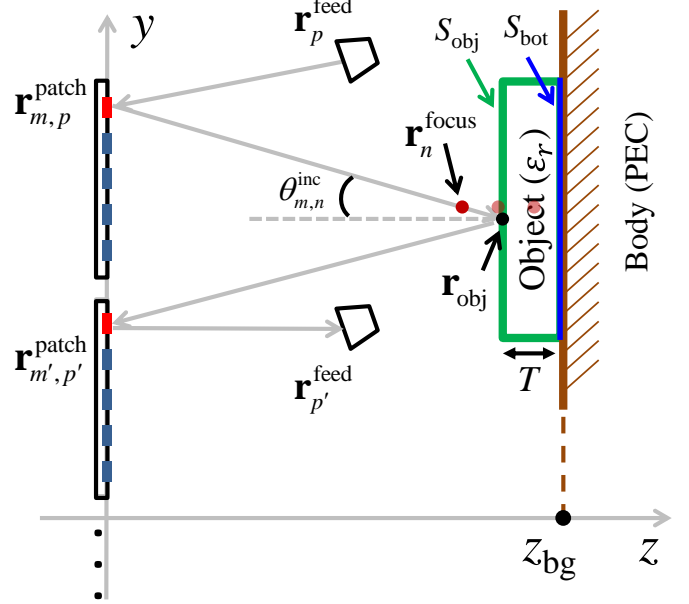


Fig. 3. GO model for the object material identification. All the rays, originating from the transmitting horns and terminating at the receiving horns, are considered for estimating the unknown complex relative permittivity ϵ_r and the thickness T . S_{obj} and S_{bot} represent the air-object and object-body interface, respectively. z_{bg} is the range of S_{bot} .

of multilevel fast multipole algorithm, MLFMA) to find the best matched magnitude and phase responses. Consequently, the corresponding estimated object thickness \hat{T} and relative permittivity $\tilde{\epsilon}_r = \tilde{\epsilon}_r' - j\tilde{\epsilon}_r''$ are obtained.

Figure 3 shows the proposed forward model for a multi-reflectarray-based system. For a general analysis, the p -th feeding antenna at $\mathbf{r}_p^{\text{feed}}$ is assumed to be active, and only the ray that originates from $\mathbf{r}_p^{\text{feed}}$ and terminates at the p' -th feeding antenna in the receiving mode at $\mathbf{r}_{p'}^{\text{feed}}$ is considered. Letting the ray at $\mathbf{r}_p^{\text{feed}}$ has an amplitude unity of E_0 , the complex incident amplitude $\tilde{E}_{m,p}^{\text{patch}}$ on the m -th patch of the p -th reflectarray can be computed by considering both magnitude loss and phase delay,

$$\tilde{E}_{m,p}^{\text{patch}} = \frac{E_0 e^{-jk_0 |\mathbf{r}_{m,p}^{\text{patch}} - \mathbf{r}_p^{\text{feed}}|}}{|\mathbf{r}_{m,p}^{\text{patch}} - \mathbf{r}_p^{\text{feed}}|}, \quad (12)$$

where $\mathbf{r}_{m,p}^{\text{patch}}$ is the position of the m -th patch of the p -th reflectarray.

Reflected from the p -th reflectarray, which is assumed to focus the CW wave at the n -th focusing point $\mathbf{r}_n^{\text{focus}}$, the ray will reach the air-object interface S_{obj} at the point \mathbf{r}_{obj} using ray tracing,

$$\mathbf{r}_{\text{obj}} = \frac{z_{\text{bg}} - T}{\cos \theta_{n,m}^{\text{inc}}} \frac{\mathbf{r}_n^{\text{focus}} - \mathbf{r}_{m,p}^{\text{patch}}}{|\mathbf{r}_n^{\text{focus}} - \mathbf{r}_{m,p}^{\text{patch}}|} + \mathbf{r}_{m,p}^{\text{patch}} \quad (13)$$

where z_{bg} is the range of the object-body interface S_{bot} ; T is the thickness of the dielectric object; and $\theta_{n,m}^{\text{inc}}$ is the incident

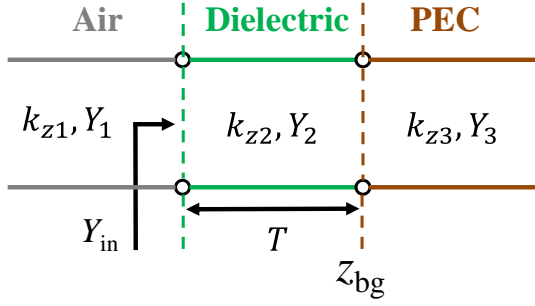


Fig. 4. Transmission line model to characterize the total reflection coefficient $\Gamma(\theta_{n,m}^{\text{inc}})$, where k_{zi} , $i \in \{1, 2, 3\}$, is the wave number in the z direction for the air, dielectric, and body (PEC) layers, respectively; Y_i is the characteristic admittance for each layer; Y_{in} is the input admittance at the air-object interface; T is the thickness of the dielectric object; and z_{bg} is the range of the object-body interface S_{bot} .

angle. Thus, the ray amplitude at \mathbf{r}_{obj} can be expressed as

$$\tilde{E}_{n,m,p}^{\text{obj}} = -\frac{\tilde{E}_{m,p}^{\text{patch}} e^{-j[k_0(|\mathbf{r}_{\text{obj}} - \mathbf{r}_{m,p}^{\text{patch}}|) - \Delta\psi_{n,m,p}]} }{1 + \left| \mathbf{r}_{\text{obj}} - \mathbf{r}_{m,p}^{\text{patch}} \right| / \left| \mathbf{r}_{m,p}^{\text{patch}} - \mathbf{r}_p^{\text{feed}} \right|}, \quad (14)$$

where $\Delta\psi_{n,m,p}$ is the binary phase shift added on the m -th patch element of the p -th reflectarray when focusing at $\mathbf{r}_n^{\text{focus}}$, which is defined in Eq. (4).

Scattered by both the dielectric and body surfaces, considering multiple reflections within the dielectric object, the backwards ray will illuminate upon the m' -th patch of the p' -th reflectarray at $\mathbf{r}_{m',p'}^{\text{patch}}$. Note that the subindexes m' and p' of $\mathbf{r}_{m',p'}^{\text{patch}}$ can be determined using ray tracing again, which are only dependent on $\mathbf{r}_{m,p}^{\text{patch}}$ and \mathbf{r}_{obj} . Thus, the ray at $\mathbf{r}_{m',p'}^{\text{patch}}$ will have an amplitude of $\tilde{E}_{p',m',n,m,p}^{\text{patch}}$,

$$\tilde{E}_{p',m',n,m,p}^{\text{patch}} = \frac{\tilde{E}_{n,m,p}^{\text{obj}} \Gamma(\theta_{n,m}^{\text{inc}}) \cdot e^{-jk_0(|\mathbf{r}_{m',p'}^{\text{patch}} - \mathbf{r}_{\text{obj}}|)}}{1 + \left| \mathbf{r}_{m',p'}^{\text{patch}} - \mathbf{r}_{\text{obj}} \right| / \left| \mathbf{r}_{\text{obj}} - \mathbf{r}_{m',p'}^{\text{patch}} \right|}, \quad (15)$$

where $\Gamma(\theta_{n,m}^{\text{inc}})$ is the total reflection coefficient at the air-object interface S_{obj} .

To characterize the total reflection coefficient $\Gamma(\theta_{n,m}^{\text{inc}})$, the transmission line model is introduced in Fig. 4. It can be an effective model because (1) the electrically large reflectarray is capable of focusing the incident wave into a tiny spot in the RoI, which is much smaller compared to the object dimensions in the transverse (x - y) plane so that the edge diffraction effect from the object can be circumvented; and (2) the dielectric object is already in the far-field region of the patch elements in the reflectarrays such that it is suitable to use the plane-wave incidence approximation in the RoI.

Denoting k_{zi} , $i \in \{1, 2, 3\}$, as the wave number in the z -direction for the air, dielectric, and body (PEC) layer, respectively, the corresponding characteristic admittance Y_i for TE and TM mode can be calculated as follows:

$$Y_i = \begin{cases} \frac{\omega \varepsilon_{ri} \varepsilon_0}{k_{zi}}, & \text{for TM mode} \\ \frac{k_{zi}}{\omega \mu_0}, & \text{for TE mode} \end{cases} \quad (16)$$

where $k_{zi} = \sqrt{k_0^2 \varepsilon_{ri} - k_x^2}$; $k_0^2 = \omega^2 \mu \varepsilon_0$; $k_x = k_0 \sin \theta_{m,n}^{\text{inc}}$; ε_0 and μ_0 are the vacuum permittivity and permeability,

respectively; and ε_{r1} , ε_{r2} , and ε_{r3} are the relative permittivities of the air, dielectric object, and PEC, respectively. The input admittance Y_{in} at the air-dielectric interface can be wrote as

$$Y_{\text{in}} = Y_2 \frac{Y_3 + jY_2 \tan k_{z2}T}{Y_2 + jY_3 \tan k_{z2}T}. \quad (17)$$

Accordingly, the total reflection coefficient $\Gamma(\theta_{n,m}^{\text{inc}})$ is expressed as

$$\Gamma(\theta_{n,m}^{\text{inc}}) = \frac{Y_1 - Y_{\text{in}}}{Y_1 + Y_{\text{in}}}. \quad (18)$$

With the confocal setup of the reflectarrays, the ray is refocused by the p' -th reflectarray and directed towards the corresponding p' -th feeding antenna located at $\mathbf{r}_{p'}^{\text{feed}}$. The received complex amplitude $\tilde{E}_{n,m,p}^{\text{rec}}$ at $\mathbf{r}_{p'}^{\text{feed}}$ is

$$\tilde{E}_{p',m',n,m,p}^{\text{rec}} = -\tilde{E}_{p',m',n,m,p}^{\text{patch}} \times \frac{e^{-j[k_0(|\mathbf{r}_{p'}^{\text{feed}} - \mathbf{r}_{m',p'}^{\text{patch}}|) - \Delta\psi_{n,m',p'}]}}{1 + \left| \mathbf{r}_{p'}^{\text{feed}} - \mathbf{r}_{m',p'}^{\text{patch}} \right| / \left| \mathbf{r}_{m',p'}^{\text{patch}} - \mathbf{r}_n^{\text{focus}} \right|}, \quad (19)$$

where $\Delta\psi_{n,m',p'}$ is the binary phase shift added on the m' -th patch element of the p' -th reflectarray when refocusing from $\mathbf{r}_n^{\text{focus}}$.

Finally, the total received complex amplitude when focusing at $\mathbf{r}_n^{\text{focus}}$ can be calculated by a summation:

$$\tilde{E}_n^{\text{rec}} = \sum_{p'=1}^P \sum_{m'=1}^M \sum_{m=1}^M \sum_{p=1}^P \tilde{E}_{p',m',n,m,p}^{\text{rec}}, \quad (20)$$

where P is the total number of FARAs; and M is the total number of patch elements at each reflectarray.

By sweeping ε_r' and ε_r'' of the relative permittivity $\varepsilon_r = \varepsilon_r' - j\varepsilon_r''$, and the thickness T , the GO predicted received amplitude $\tilde{E}_n^{\text{rec}}(\varepsilon_r', \varepsilon_r'', T)$, $n \in [1, N]$, N being the total number of focusing points used in the estimation, are calculated, and compared to the measured E_n^{rec} to find the best match by means of minimizing the error function $f(\varepsilon_r', \varepsilon_r'', T)$, namely

$$\begin{aligned} \{\tilde{\varepsilon}_r', \tilde{\varepsilon}_r'', \tilde{T}\} &= \arg \min_{\varepsilon_r', \varepsilon_r'', T} \{f(\varepsilon_r', \varepsilon_r'', T)\} \\ \text{s.t. } f(\varepsilon_r', \varepsilon_r'', T) &= \sum_{n=1}^N \left| \frac{\tilde{E}_n^{\text{rec}}}{E_0^{\text{rec}}} - \frac{E_n^{\text{rec}}}{E_0^{\text{rec}}} \right|, \end{aligned} \quad (21)$$

where $\tilde{\varepsilon}_r'$, $\tilde{\varepsilon}_r''$, and \tilde{T} are the estimated object dielectric constant, loss factor, and thickness, respectively; and \tilde{E}_0^{rec} and E_0^{rec} are the calibration amplitudes to normalize the predicted and measured received fields, respectively, which are independent on the dielectric object under detection, and can be measured by focusing the incident wave at a reference plane, located at a range different from or the same as z_{bg} .

IV. PRIMARY RESULTS

To validate the proposed method for object profiles reconstruction and materials identification, both simulated and experimental examples are examined. The simulation setup is the same as that in the experiment, which is shown in Fig. 5. Each reflectarray has a side length of 1000 mm. The centers of the top and the bottom reflectarray are located at

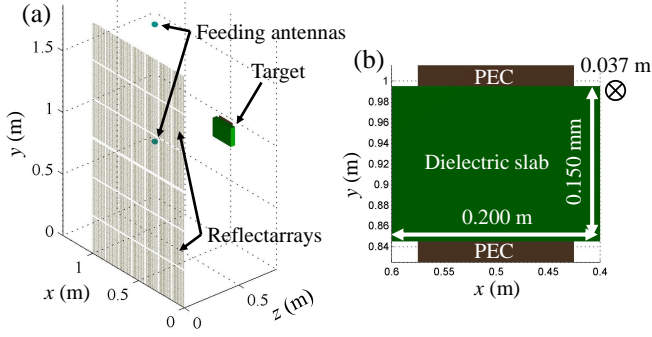


Fig. 5. 3D setup for simulation and experiment: (a) two reflectarrays are vertically stacked and fed by two 10 dB standard gain pyramidal horn antennas, operated at 24.16 GHz; and (b) the dielectric object is attached to the center of the PEC plate.

[500, 1413, 0] mm and [500, 461, 0] mm, respectively. Two identical 10 dB standard gain pyramidal horn antennas are placed at [1313, 1413, 830] mm and [1313, 461, 830] mm, respectively, facing the corresponding centers of the reflectarrays. The horn antennas are operated at the single frequency 24.16 GHz, corresponding to a wavelength of $\lambda_0 \approx 12.4$ mm. The dielectric object is a slab that is attached to the center [500, 920, 800] mm of a steel plate ($z_{bg} = 800$ mm). The slab has the dimensions of 200 mm, 150 mm, and 37 mm in the x -, y -, and z -axis, respectively. Note that the object thickness can be varied in different simulated and experimental cases.

A. Simulation Results

First of all, it is important to examine the focusing quality of the reflectarrays based on the point spread function (PSF) [57]. By setting the focusing point at [500, 920, 800] mm in free-space, the PSF is calculated. Figure 6(a) and 6(b) show the 3D and 2D radiation patterns, respectively. As anticipated, a sharp focusing spot, namely high imaging resolution, is achieved. The 3-dB width of the focusing spot is near $\lambda_0/2$ along the x - and y -axis, and λ_0 along the z -axis.

In order to obtain a high calculation efficiency while retaining an acceptable imaging accuracy, the 3rd-order PO is used to calculate the electric and magnetic currents on the dielectric object surface, namely applying Eq. (7) with $K = 3$.

First, two pure dielectric (lossless) objects are considered in the simulation. Object-1 has a thickness of $T_1 = 20$ mm and relative permittivity of $\epsilon_{r1} = 8.0 - j0.0$; while Object-2 has a thickness of $T_2 = 40$ mm and relative permittivity of $\epsilon_{r2} = 2.0 - j0.0$. These two objects, satisfying $T_1 \sqrt{\epsilon'_{r1}} = T_2 \sqrt{\epsilon'_{r2}}$, are selected to verify that the proposed method is able to solve the phase-shift ambiguity [45] without loss of generality.

In addition, the general reciprocity theorem described in Eq. (9) are applied throughout the simulations to improve the computation efficiency. Its effectiveness is validated in Fig. 7, where the received fields, with and without the reciprocity theorem, are in a good agreement for both Object-1 and Object-2. Figure 7 also verifies that the radiation pattern of the reflectarray in the near-field is range-dependent so that the magnitude and phase responses of the received fields for the two ambiguous objects are distinguished, which shows

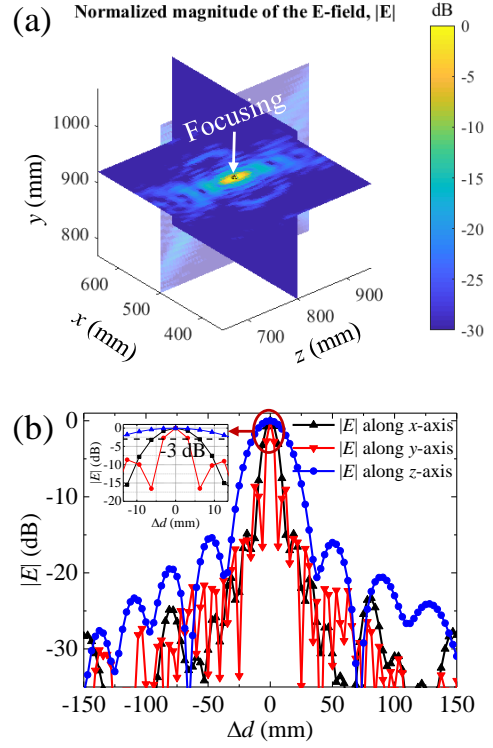


Fig. 6. PSF of the reflectarray imaging system when the focusing is at [500, 920, 800] mm in free-space. (a) and (b) show the 3D and 2D radiation patterns, respectively. Δd is the distance between the focusing point and the observation point.

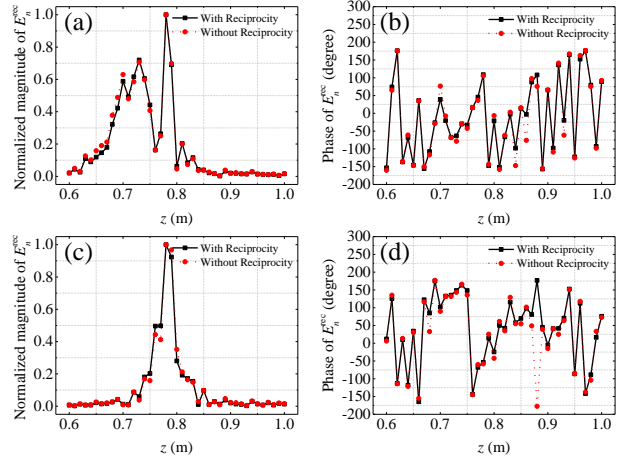


Fig. 7. Received field, with and without applying the reciprocity theorem, for the simulation setup described in Fig. 5. The focusing point is uniformly swept from [500, 920, 600] mm to [500, 920, 1000] mm along the z -axis. (a) and (b) are the calculated magnitude and phase distribution, respectively, for Object-1; and, similarly, (c) and (d) are the calculated magnitude and phase distribution, respectively, for Object-2.

the effectiveness to discriminate these two objects using the algorithm derived in Eq. (21).

Figure 8(a) and 8(b) show the PO simulated target profiles for Object-1 and Object-2, respectively, which give the accurate widths, in the x -axis, and heights, in the y -axis, for both Object-1 and Object-2. As it is also seen, for Object-1

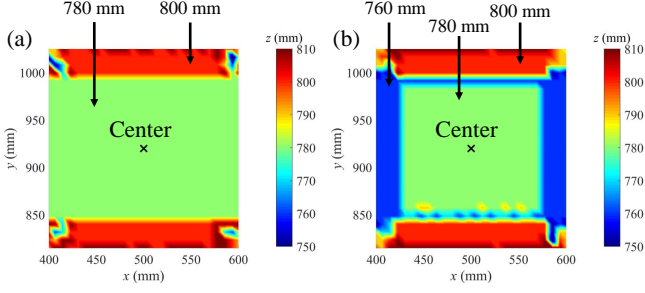


Fig. 8. (a) PO simulated target profile for Object-1 ($\epsilon_{r1} = 8.0 - j0.0$ and $T_1 = 20$ mm), where the imaged thickness and profile center are 20 mm and $[x_{c1}, y_{c1}, z_{c1}] = [500, 920, 780]$ mm, respectively; and (b) PO simulated target profile for Object-2 ($\epsilon_{r2} = 2.0 - j0.0$ and $T_2 = 40$ mm), where the imaged thickness and profile center are 20 mm and $[x_{c2}, y_{c2}, z_{c2}] = [500, 920, 780]$ mm, respectively.

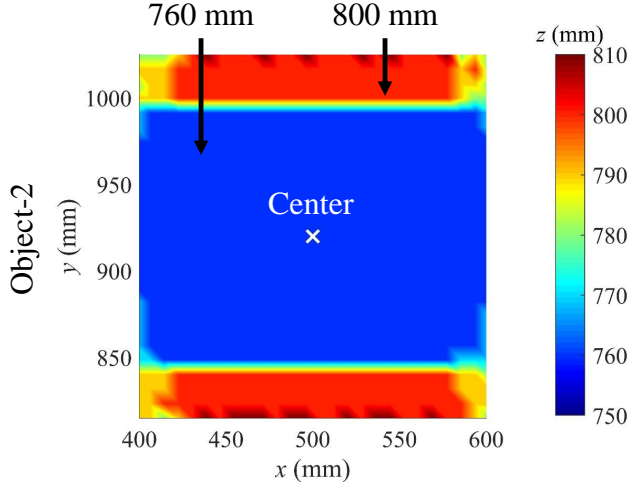


Fig. 9. PO simulated target profile for Object-3 ($\epsilon_{r3} = 4.0 - j0.2$ and $T_3 = 40$ mm), where the imaged thickness and profile center are 40 mm and $[x_{c3}, y_{c3}, z_{c3}] = [500, 920, 760]$ mm, respectively.

with an actual thickness of 20 mm, the imaged profile center and thickness are $[x_{c1}, y_{c1}, z_{c1}] = [500, 920, 780]$ mm and $800 - 780 = 20$ mm, respectively; however, for Object-2 that has an actual thickness of 40 mm, the imaged profile center and thickness are also $[x_{c2}, y_{c2}, z_{c2}] = [500, 920, 780]$ mm and $800 - 780 = 20$ mm, respectively. This phenomenon is attributed to the multiple reflections inside the dielectric object so that the focusing position, corresponding to the maximum magnitude of the received field along the z -axis, is achieved under the front surface of the dielectric object.

When it occurs to a lossy Object-3, assuming it has a thickness of $T_3 = 40$ mm and complex relative permittivity of $\epsilon_{r3} = 4.0 - j0.2$, the magnitude of the multiple reflected waves inside the lossy dielectric slab are considerably degenerated due to the large propagation loss, $\epsilon_r'' = 0.2$. The imaging processing of Object-3 can be similar to that of a metallic object, where the 1st-order PO method can be sufficient to obtain a quite accurate target profile, and the maximum received field along z -axis can be achieved when the focusing position is near the front surface of the dielectric object. Figure 9 shows the PO simulated profile of Object-3, where

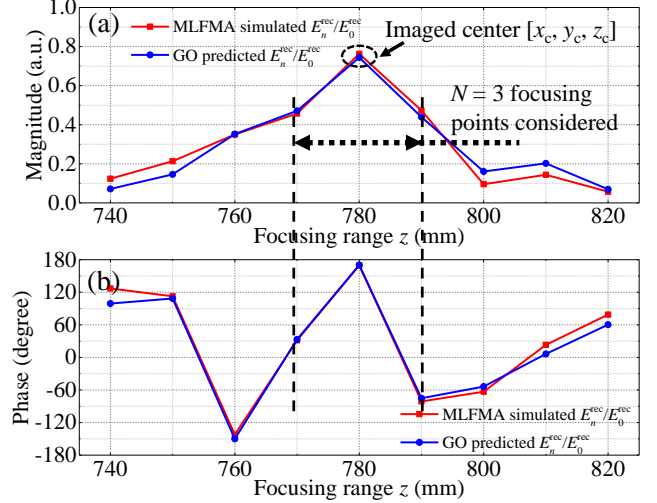


Fig. 10. Best matched magnitude (a) and phase (b) response for Object-1, when the minimum error $\min\{f(\epsilon_r', \epsilon_r'', T)\}$ is achieved at $\tilde{\epsilon}_r' = 8.0$, $\tilde{\epsilon}_r'' = 0.0$, and $\tilde{T} = 20$ mm.

the imaged profile center and thickness are $[x_{c3}, y_{c3}, z_{c3}] = [500, 920, 760]$ mm and $800 \text{ mm} - 760 \text{ mm} = 40$ mm, respectively.

Considering all aforementioned simulation cases, for an object made of unknown material, a further estimation algorithm, in addition to the profile reconstruction, is required to estimate not only the object permittivity but also a more precise object thickness.

Applying the material identification method derived in Section III-B, ϵ_r' and ϵ_r'' are swept from 2.0 to 10.0, and from 0 to 0.5, respectively. This sweep range covers most common threat materials, such as narcotics, explosives, and other types of contrabands [58], [59]. The dielectric slab thickness T is swept from 0 mm to 60 mm. By determining the imaged profile center $[x_c, y_c, z_c]$ for each object, the equally spaced focusing points can be selected along the range (z -axis),

$$\mathbf{r}_n^{\text{focus}} = \left[x_c, y_c, z_c + \Delta z \left(n - \frac{N+1}{2} \right) \right], n \in [1, N], \quad (22)$$

where $\Delta z = 10$ mm is the range resolution of the RoI, and total $N = 3$ focusing points are considered for estimating object thickness \tilde{T} and complex relative permittivity $\tilde{\epsilon}_r = \tilde{\epsilon}_r' - j\tilde{\epsilon}_r''$. The importance for selecting those focusing points is that they always correspond to higher receiving magnitudes compared to the other focusing points along the z -axis; therefore, a higher receiving signal-to-noise ratio (SNR) can be achieved for a better estimation accuracy.

As it is shown in Fig. 10, the best matched magnitude (a) and phase (b) responses, corresponding to the minimum error $\min\{f(\epsilon_r', \epsilon_r'', T)\}$, for Object-1 are found at $\tilde{\epsilon}_r' = 8.0$, $\tilde{\epsilon}_r'' = 0.0$, and $\tilde{T} = 20$ mm. These estimated parameters are the same as the actual object thickness and relative permittivity. Note that, although more than three focusing points are presented in this figure for the purpose of verifying the accuracy of the GO predicted field, only the highlighted middle three points are utilized for the estimation. The error distribution $f(\epsilon_r', \epsilon_r'', T)$, obtained when sweeping ϵ_r' , ϵ_r'' , and

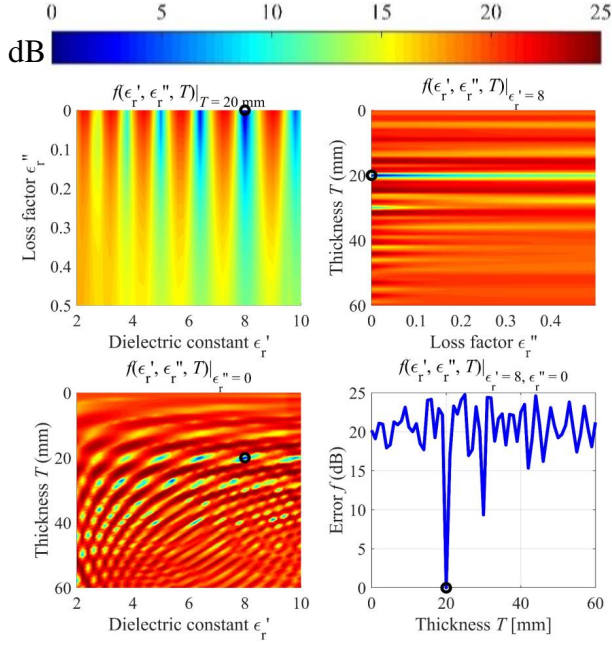


Fig. 11. Error distribution $f(\varepsilon_r', \varepsilon_r'', T)$ for Object-1, obtained by sweeping $\varepsilon_r', \varepsilon_r''$, and T , where the achieved minimum error is denoted by a circle.

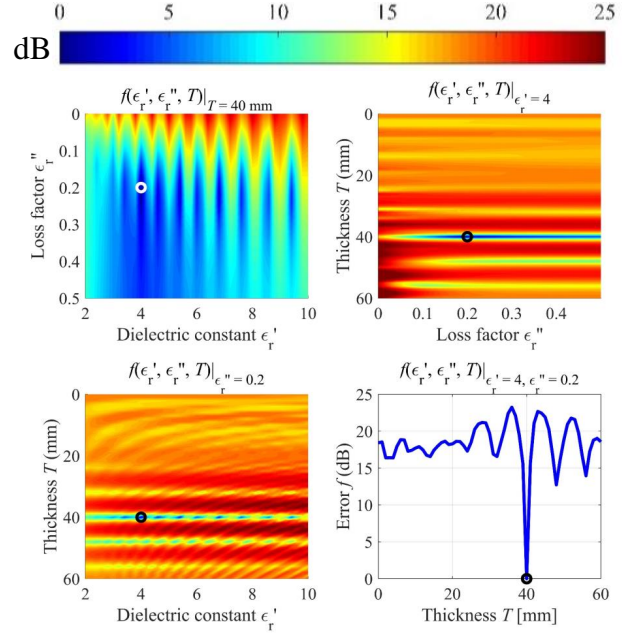


Fig. 13. Error distribution $f(\varepsilon_r', \varepsilon_r'', T)$ for Object-3, obtained by sweeping $\varepsilon_r', \varepsilon_r''$, and T , where the achieved minimum error is denoted by a circle.

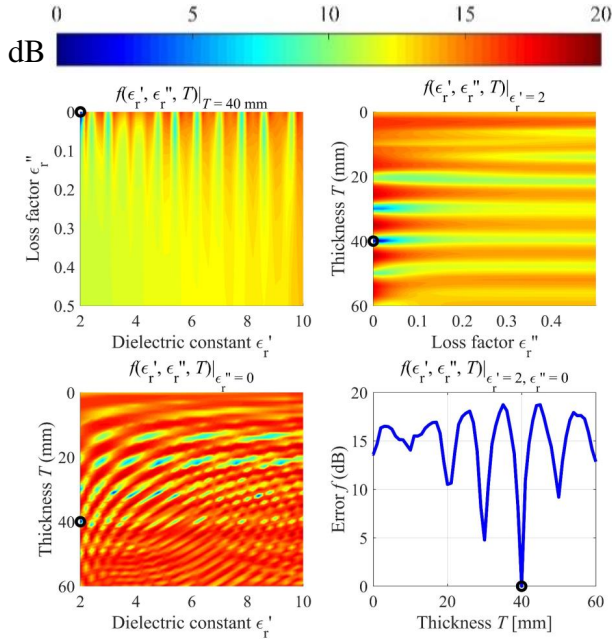


Fig. 12. Error distribution $f(\varepsilon_r', \varepsilon_r'', T)$ for Object-2, obtained by sweeping $\varepsilon_r', \varepsilon_r''$, and T , where the achieved minimum error is denoted by a circle.

T , are shown in Fig. 11, where the achieved minimum error is denoted by a circle. The same estimation process is performed for Object-2, and the obtained error distribution is shown in Fig. 12. As it is seen, the minimum error $\min\{f(\varepsilon_r', \varepsilon_r'', T)\}$ also converges to the actual object parameters $\tilde{\varepsilon}_r' = 2.0$, $\tilde{\varepsilon}_r'' = 0.0$, and $\tilde{T} = 40$ mm. Therefore, these two ambiguous objects are distinguishable from each other using the proposed estimation method. The error distribution $f(\varepsilon_r', \varepsilon_r'', T)$ for the lossy Object-3 are shown in Fig. 13, where the minimum error is achieved at $\tilde{\varepsilon}_r' = 4.0$, $\tilde{\varepsilon}_r'' = 0.2$, and $\tilde{T} = 40$ mm,

converging to the actual object parameters again. Accordingly, aforementioned simulation examples and results verify the proposed imaging scheme that is able to not only image the profiles but also effectively retrieve the complex relative permittivities of the dielectric objects, where a precise object thicknesses can be estimated.

B. Experimental Results

The actual experiment setup to detect a threat object is given in Fig. 14. Denote the dielectric object as Object-4. It is a dielectric slab made of polyamide-6, 6 (PA66), which has a relative dielectric constant of $2.8 \sim 3.1$ and a low loss tangent of $\tan \sigma < 0.01$ at K -band [60]. The size of the dielectric is $200 \text{ mm} \times 150 \text{ mm} \times 37 \text{ mm}$. The dielectric slab is attached to the center of a steel plate by a 1.0 mm ($< \lambda_0/10$) Velcro layer. To predict the received amplitude $\tilde{E}_n^{\text{rec}}(\varepsilon_r', \varepsilon_r'', T)$ using GO forward model described in Fig. 3, the Velcro layer is approximated to be an layer of air with the same thickness 1.0 mm . Therefore, the transmission line model in Fig. 4 for calculating the total reflection coefficient $\Gamma(\theta_{n,m}^{\text{inc}})$ is modified, which includes four cascaded layers, namely air-dielectric-air-PEC.

Figure 15 shows the experimentally reconstructed target profile, which has an imaged thickness of 20 mm that is much smaller than the actual thickness of 37 mm . The imaged profile center is at $[500, 920, 780] \text{ mm}$. The reason for this is that the strong multiple reflections within the dielectric slab make the focusing position, corresponding to the maximum magnitude of the received field along the z -axis, achieved under the front surface of the dielectric object. This explanation is the same as that for the simulation results in Fig. 8(b).

To estimate the complex relative permittivity $\tilde{\varepsilon}_r = \tilde{\varepsilon}_r' - j\tilde{\varepsilon}_r''$ and a more precise thickness \tilde{T} of the PA66 slab, $\varepsilon_r', \varepsilon_r''$, and

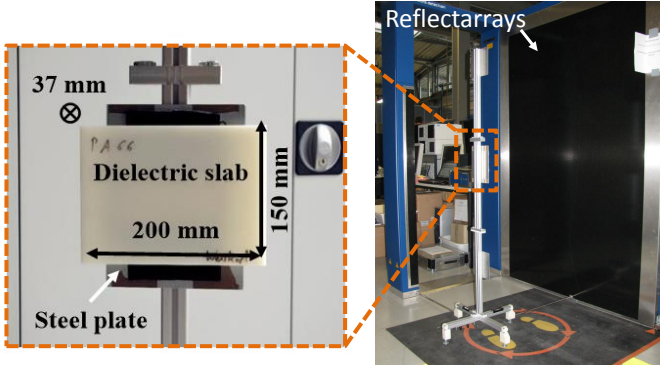


Fig. 14. Experimental setup to detect a dielectric object. The material of the dielectric is made of polyamide-6, 6 (PA66). The size of the dielectric is 200 mm \times 150 mm \times 37 mm, which is attached to the center of the steel plate.

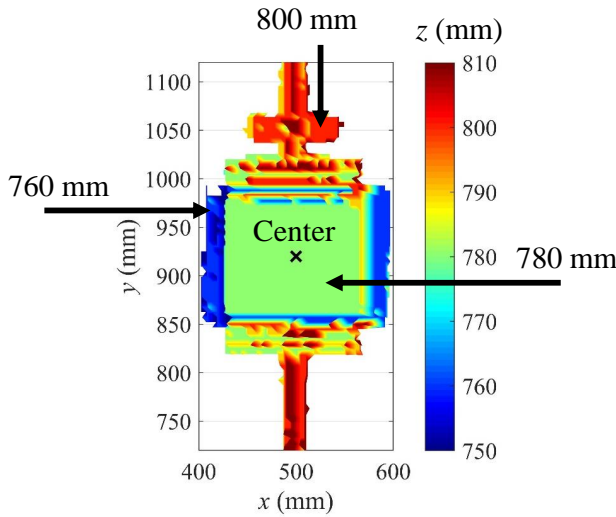


Fig. 15. Experimentally reconstructed target profile, where the imaged thickness and profile center are 20 mm and $[x_{c4}, y_{c4}, z_{c4}] = [500, 920, 780]$ mm, respectively.

T are swept to compute the GO predicted received amplitude $\tilde{E}_n^{\text{rec}}(\tilde{\epsilon}'_r, \tilde{\epsilon}''_r, \tilde{T})$, which are then compared to the experimental measurements E_n^{rec} to find the best matched magnitude and phase responses using Eq.(21). The measurement is performed 38 times and 3 focusing points are considered. Figure 16 shows the best matched magnitude (a) and phase (b) responses between the measured electric fields E_n^{rec} and GO predicted $\tilde{E}_n^{\text{rec}}(\tilde{\epsilon}'_r, \tilde{\epsilon}''_r, \tilde{T})$, corresponding to the minimum error $\min \{f(\tilde{\epsilon}'_r, \tilde{\epsilon}''_r, \tilde{T})\}$. As we can see, the received field magnitude E_2^{rec} , corresponding to the focusing point at the range $z = 780$ mm, has the maximum magnitude compared to the measured magnitudes of the other focusing points along the z -axis. This is accordance with the experimentally reconstructed target profile, shown in Fig. 15, where the imaged object front surface is located at the range $z = 780$ mm.

The estimated results on $\tilde{\epsilon}'_r$, $\tilde{\epsilon}''_r$, and \tilde{T} of the PA66 slab are given in Fig. 17. As shown in Table I, the mean values for $\tilde{\epsilon}'_r$, $\tilde{\epsilon}''_r$, and \tilde{T} are 3.012, 0.014, and 37.6 mm, respectively; and the standard deviations for $\tilde{\epsilon}'_r$, $\tilde{\epsilon}''_r$, and \tilde{T} are 0.425, 0.009, and 0.593 mm, respectively. The estimation error can

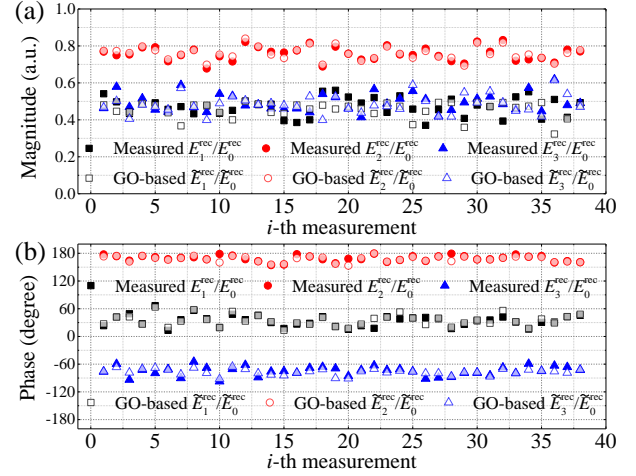


Fig. 16. The best matched magnitude (a) and phase (b) responses between the measured electric fields E_n^{rec} and GO predicted \tilde{E}_n^{rec} , where the three considered focusing points are defined in Eq. (22) with $N = 3$.

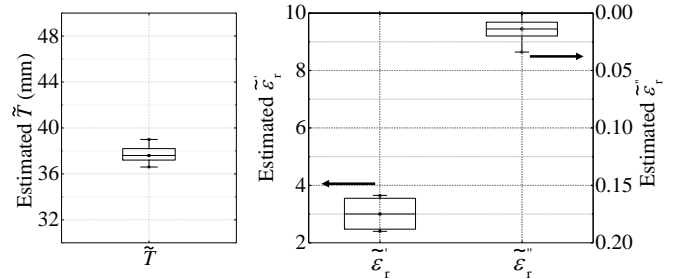


Fig. 17. Experimentally estimated dielectric constant $\tilde{\epsilon}'_r$, loss factor $\tilde{\epsilon}''_r$, and thickness \tilde{T} of the PA66 dielectric slab.

TABLE I
ESTIMATED RESULTS ON THE THICKNESS \tilde{T} AND COMPLEX RELATIVE PERMITTIVITY $\tilde{\epsilon}_r = \tilde{\epsilon}'_r - j\tilde{\epsilon}''_r$ FOR THE PA66 SLAB

Values	\tilde{T}	$\tilde{\epsilon}'_r$	$\tilde{\epsilon}''_r$
Mean	37.6 mm	3.012	0.014
Standard deviation	0.593 mm	0.425	0.009

be attributed to the noisy experimental measurement as well as the approximated model of the four-layer transmission line.

V. CONCLUSION

A physical and geometrical optics imaging algorithm is derived for profile reconstruction and material identification in multiple reconfigurable reflectarrays based people-screening systems. Both simulations and experimental validations are carried out to examine the feasibility. Preliminary results show that the imaging system is able to not only reconstruct the target profile, but also characterize the complex relative permittivity of the dielectric object.

When accessible to a well defined database including the knowledge of the permittivities of typical threat materials, the proposed imaging scheme is capable of suggesting threat

identities based on the estimated permittivities. This imaging scheme can have a variety of applications in security screening checkpoints at train stations, airports, concerts, sporting events, government buildings, and many other public and private facilities to predict potential threats.

ACKNOWLEDGMENT

This work is funded by the U.S. Department of Homeland Security, Award No. 2013-ST-061-ED0001. The authors would like to thank Smiths Detection for collecting the data with their Ego system.

REFERENCES

- [1] D. M. Sheen, D. L. McMakin, and T. E. Hall, "Three-dimensional millimeter-wave imaging for concealed weapon detection," *IEEE Trans. Microw. Theory Tech.*, vol. 49, no. 9, pp. 1581–1592, Sep 2001.
- [2] S. S. Ahmed, A. Schiessl, and L. P. Schmidt, "A novel fully electronic active real-time imager based on a planar multistatic sparse array," *IEEE Trans. Microw. Theory Tech.*, vol. 59, no. 12, pp. 3567–3576, Dec 2011.
- [3] S. S. Ahmed, A. Schiessl, F. Gumbmann, M. Tiebout, S. Methfessel, and L. P. Schmidt, "Advanced microwave imaging," *IEEE Microw. Mag.*, vol. 13, no. 6, pp. 26–43, Sept 2012.
- [4] J. A. Martinez-Lorenzo, F. Quivira, and C. M. Rappaport, "Sar imaging of suicide bombers wearing concealed explosive threats," *Progress in Electromagnetics Research*, vol. 125, pp. 255–272, 2012.
- [5] Y. Rodriguez-Vaqueiro, Y. lvarez Lpez, B. Gonzlez-Valdes, J. . Martnez, F. Las-Heras, and C. M. Rappaport, "On the use of compressed sensing techniques for improving multistatic millimeter-wave portal-based personnel screening," *IEEE Trans. Antennas Propag.*, vol. 62, no. 1, pp. 494–499, Jan 2014.
- [6] P. M. Meaney, K. D. Paulsen, A. Hartov, and R. K. Crane, "Microwave imaging for tissue assessment: initial evaluation in multitarget tissue-equivalent phantoms," *IEEE Trans. Biomed. Eng.*, vol. 43, no. 9, pp. 878–890, Sept. 1996.
- [7] P. M. Meaney, M. W. Fanning, D. Li, S. P. Poplack, and K. D. Paulsen, "A clinical prototype for active microwave imaging of the breast," *IEEE Trans. Microw. Theory Tech.*, vol. 48, no. 11, pp. 1841–1853, Nov. 2000.
- [8] E. C. Fear, X. Li, S. C. Hagness, and M. A. Stuchly, "Confocal microwave imaging for breast cancer detection: localization of tumors in three dimensions," *IEEE Trans. Biomed. Eng.*, vol. 49, no. 8, pp. 812–822, Aug 2002.
- [9] L. Yujiri, M. Shoucri, and P. Moffa, "Passive millimeter wave imaging," *IEEE Microw. Mag.*, vol. 4, no. 3, pp. 39–50, Sept 2003.
- [10] M. Benedetti, M. Donelli, A. Martini, M. Pastorino, A. Rosani, and A. Massa, "An innovative microwave-imaging technique for nondestructive evaluation: Applications to civil structures monitoring and biological bodies inspection," *IEEE Trans. Instrum. Meas.*, vol. 55, no. 6, pp. 1878–1884, Dec 2006.
- [11] T. Slesman, M. Boyarsky, M. F. Imani, T. Fromenteze, J. N. Gollub, and D. R. Smith, "Single-frequency microwave imaging with dynamic metasurface apertures," *J. Opt. Soc. Am. B*, vol. 34, no. 8, pp. 1713–1726, Aug 2017.
- [12] J. C. Bolomey, "Recent european developments in active microwave imaging for industrial, scientific, and medical applications," *IEEE Trans. Microw. Theory Tech.*, vol. 37, no. 12, pp. 2109–2117, Dec 1989.
- [13] B. D. Steinberg and H. M. Subbaram, *Microwave imaging techniques*. John Wiley & Sons, 1991.
- [14] S. R. Cloude and E. Pottier, "A review of target decomposition theorems in radar polarimetry," *IEEE Trans. Geosci. Remote Sens.*, vol. 34, no. 2, pp. 498–518, Mar 1996.
- [15] E. C. Fear, J. Bourqui, C. Curtis, D. Mew, B. Docktor, and C. Romano, "Microwave breast imaging with a monostatic radar-based system: A study of application to patients," *IEEE Trans. Microw. Theory Tech.*, vol. 61, no. 5, pp. 2119–2128, May 2013.
- [16] I. Walterscheid, J. H. G. Ender, A. R. Brenner, and O. Loffeld, "Bistatic sar processing and experiments," *IEEE Trans. Geosci. Remote Sens.*, vol. 44, no. 10, pp. 2710–2717, Oct 2006.
- [17] G. Krieger and A. Moreira, "Spaceborne bi- and multistatic sar: potential and challenges," *IEE Proceedings - Radar, Sonar and Navigation*, vol. 153, no. 3, pp. 184–198, June 2006.
- [18] J. S. Herd and M. D. Conway, "The evolution to modern phased array architectures," *Proc. IEEE*, vol. 104, no. 3, pp. 519–529, Mar. 2016.
- [19] D. L. Donoho, "Compressed sensing," *IEEE Trans. Inf. Theory*, vol. 52, no. 4, pp. 1289–1306, Apr. 2006.
- [20] M. T. Alonso, P. Lopez-Dekker, and J. J. Mallorqui, "A novel strategy for radar imaging based on compressive sensing," *IEEE Trans. Geosci. Remote Sens.*, vol. 48, no. 12, pp. 4285–4295, Dec 2010.
- [21] M. Soumekh, *Synthetic Aperture Radar Signal Processing*. Wiley, 1999.
- [22] P. Corredoura, Z. Baharav, B. Taber, and G. Lee, "Millimeter-wave imaging system for personnel screening: scanning 10^7 points a second and using no moving parts," *Proc. SPIE*, vol. 6211, pp. 6211 – 6211 – 8, 2006.
- [23] B. N. Lyons, E. Entchev, and M. K. Crowley, "Reflect-array based mm-wave people screening system," *Proc. SPIE*, vol. 8900, pp. 8900 – 8900 – 10, 2013.
- [24] H. Gomez-Sousa and J. A. Martinez-Lorenzo, "Modeling and imaging security threats using a single-frequency adaptable reflect-array," in *Proc. 2017 IEEE International Symposium on Technologies for Homeland Security (HST)*, Apr. 2017, pp. 1–7.
- [25] M. B. Abdilllah, B. Lyons, and E. Entchev, "Identification of potential threat materials using active electromagnetic waves," Mar. 5 2013, uS Patent 8,390,504.
- [26] J. Huang, "Microstrip reflectarray," in *Antennas and Propagation Society Symposium 1991 Digest*, June 1991, pp. 612–615 vol.2.
- [27] D. M. Pozar, S. D. Targonski, and H. D. Syrigos, "Design of millimeter wave microstrip reflectarrays," *IEEE Trans. Antennas Propag.*, vol. 45, no. 2, pp. 287–296, Feb 1997.
- [28] W. Baukus, "X ray imaging for on-the-body contraband detection," in *Proc. 16th Annual Security Technology Symposium & Exhibition*, 2000.
- [29] S. Ahmed, F. Gumbmann, A. Schiessl, M. Reiband, S. Methfessel, C. Maire, A. Cenanovic, O. Ostwald, C. Evers, and L. Schmidt, "Qpass quick personnel automatic safe screening for security enhancement of passengers," in *Proc. Future Security Conf.*, 2011.
- [30] O. Yurduseven, "Indirect microwave holographic imaging of concealed ordnance for airport security imaging systems," *Progress In Electromagnetics Research*, vol. 146, pp. 7–13, 2014.
- [31] B. Gonzalez-Valdes, Y. Alvarez-Lopez, J. A. Martinez-Lorenzo, F. L. H. Andres, and C. M. Rappaport, "Sar processing for profile reconstruction and characterization of dielectric objects on the human body surface," *Progress In Electromagnetics Research*, vol. 138, pp. 269–282, 2013.
- [32] Y. Alvarez, B. Gonzalez-Valdes, J. A. Martinez-Lorenzo, C. M. Rappaport, and F. Las-Heras, "Sar imaging-based techniques for low permittivity lossless dielectric bodies characterization," *IEEE Antennas Propag. Mag.*, vol. 57, no. 2, pp. 267–276, Apr. 2015.
- [33] J. C. Weatherall, J. Barber, and B. T. Smith, "Spectral signatures for identifying explosives with wideband millimeter-wave illumination," *IEEE Trans. Microw. Theory Tech.*, vol. 64, no. 3, pp. 999–1005, Mar. 2016.
- [34] M. E. Baginski, D. L. Faircloth, and M. D. Deshpande, "Comparison of two optimization techniques for the estimation of complex permittivities of multilayered structures using waveguide measurements," *IEEE Trans. Microw. Theory Tech.*, vol. 53, no. 10, pp. 3251–3259, Oct 2005.
- [35] A. Zamani and A. M. Abbosh, "Estimation of frequency dispersive complex permittivity seen by each antenna for enhanced multistatic radar medical imaging," *IEEE Trans. Antennas Propag.*, vol. 65, no. 7, pp. 3702–3711, July 2017.
- [36] D. W. Winters, E. J. Bond, B. D. V. Veen, and S. C. Hagness, "Estimation of the frequency-dependent average dielectric properties of breast tissue using a time-domain inverse scattering technique," *IEEE Trans. Antennas Propag.*, vol. 54, no. 11, pp. 3517–3528, Nov 2006.
- [37] K. K. M. Chan, A. E. C. Tan, L. Li, and K. Rambabu, "Material characterization of arbitrarily shaped dielectrics based on reflected pulse characteristics," *IEEE Trans. Microw. Theory Tech.*, vol. 63, no. 5, pp. 1700–1709, May 2015.
- [38] J. Bourqui and E. C. Fear, "System for bulk dielectric permittivity estimation of breast tissues at microwave frequencies," *IEEE Trans. Microw. Theory Tech.*, vol. 64, no. 9, pp. 3001–3009, Sept 2016.
- [39] B. J. Mohammed, K. S. Bialkowski, and A. M. Abbosh, "Radar-based time-domain head imaging using database of effective dielectric constant," *Electron. Lett.*, vol. 51, no. 20, pp. 1574–1576, 2015.
- [40] S. Salman, D. Psychoudakis, and J. L. Volakis, "Determining the relative permittivity of deep embedded biological tissues," *IEEE Antennas Wireless Propag. Lett.*, vol. 11, pp. 1694–1697, 2012.
- [41] M. A. Islam, A. Kiourt, and J. L. Volakis, "A novel method of deep tissue biomedical imaging using a wearable sensor," *IEEE Sensors J.*, vol. 16, no. 1, pp. 265–270, Jan 2016.
- [42] W. B. Weir, "Automatic measurement of complex dielectric constant and permeability at microwave frequencies," *Proc. IEEE*, vol. 62, no. 1, pp. 33–36, Jan 1974.

- [43] R. A. Fenner, E. J. Rothwell, and L. L. Frasc, "A comprehensive analysis of free-space and guided-wave techniques for extracting the permeability and permittivity of materials using reflection-only measurements," *Radio Sci.*, vol. 47, no. 01, pp. 1–13, Feb. 2012.
- [44] P. Nayeri, A. Z. Elsherbeni, and F. Yang, "Radiation analysis approaches for reflectarray antennas [antenna designer's notebook]," *IEEE Antennas Propag. Mag.*, vol. 55, no. 1, pp. 127–134, Feb. 2013.
- [45] S. Trabelsi, A. W. Kraszewski, and S. O. Nelson, "Phase-shift ambiguity in microwave dielectric properties measurements," *IEEE Trans. Instrum. Meas.*, vol. 49, no. 1, pp. 56–60, Feb. 2000.
- [46] J. Roelvink and S. Trabelsi, "Measuring the complex permittivity of thin grain samples by the free-space transmission technique," in *2012 IEEE International Instrumentation and Measurement Technology Conference Proceedings*, May 2012, pp. 310–313.
- [47] K. Y. You, M. S. Sim, H. Mutadza, F. Esa, and Y. L. Chan, "Free-space measurement using explicit, reference-plane and thickness-invariant method for permittivity determination of planar materials," in *2017 Progress in Electromagnetics Research Symposium - Fall (PIERS - FALL)*, Nov 2017, pp. 222–228.
- [48] S. V. Hum, M. Okoniewski, and R. J. Davies, "Realizing an electronically tunable reflectarray using varactor diode-tuned elements," *IEEE Microw. Wirel. Compon. Lett.*, vol. 15, no. 6, pp. 422–424, June 2005.
- [49] E. Carrasco, M. Barba, and J. A. Encinar, "X-band reflectarray antenna with switching-beam using pin diodes and gathered elements," *IEEE Trans. Antennas Propag.*, vol. 60, no. 12, pp. 5700–5708, Dec 2012.
- [50] H. Theissen, C. Dahl, I. Rolfes, and T. Musch, "An electronically reconfigurable reflectarray element based on binary phase shifters for k-band applications," in *Proc. 2016 German Microwave Conference (GeMiC)*, March 2016, pp. 321–324.
- [51] C. A. Balanis, *Advanced Engineering Electromagnetics, 2nd ed.* Wiley, 2012.
- [52] J. G. Meana, J. . Martinez-Lorenzo, F. Las-Heras, and C. Rappaport, "Wave scattering by dielectric and lossy materials using the modified equivalent current approximation (meca)," *IEEE Trans. Antennas Propag.*, vol. 58, no. 11, pp. 3757–3761, Nov 2010.
- [53] J. Gutiérrez-Meana, J. Á. Martínez-Lorenzo, and F. Las-Heras, "High frequency techniques: The physical optics approximation and the modified equivalent current approximation (meca)," in *Electromagnetic waves propagation in complex matter*. InTech, 2011.
- [54] R. G. Kouyoumjian and P. H. Pathak, "A uniform geometrical theory of diffraction for an edge in a perfectly conducting surface," *Proc. IEEE*, vol. 62, no. 11, pp. 1448–1461, Nov. 1974.
- [55] P. H. Pathak and R. G. Kouyoumjian, "An analysis of the radiation from apertures in curved surfaces by the geometrical theory of diffraction," *Proc. IEEE*, vol. 62, no. 11, pp. 1438–1447, Nov 1974.
- [56] W. Zhang and J. A. Martinez-Lorenzo, "Single-frequency material characterization using a microwave adaptive reflect-array," in *2018 IEEE International Symposium on Antennas and Propagation USNC/URSI National Radio Science Meeting*, July 2018, pp. 1063–1064.
- [57] P. J. Shaw and D. J. Rawlins, "The point-spread function of a confocal microscope: its measurement and use in deconvolution of 3-d data," *Journal of Microscopy*, vol. 163, no. 2, pp. 151–165, 1991. [Online]. Available: <http://dx.doi.org/10.1111/j.1365-2818.1991.tb03168.x>
- [58] D. G. Watters, D. G. Falconer, K. J. Harker, R. Ueberschaer, and A. J. Bahr, "Microwave inspection of luggage for contraband materials using imaging and inverse-scattering algorithms," *Research in Nondestructive Evaluation*, vol. 7, no. 2, pp. 153–168, Jun 1995.
- [59] E. M. Hussein and E. J. Waller, "Review of one-side approaches to radiographic imaging for detection of explosives and narcotics," *Radiation Measurements*, vol. 29, no. 6, pp. 581 – 591, 1998.
- [60] A. R. Von Hippel, *Dielectric materials and applications*. New York: Wiley, 1954.